

Cohesive-Shear-Lag Modeling of Interfacial Stress Transfer Between a Monolayer Graphene and a Polymer Substrate

Guodong Guo

Department of Mechanical and Aerospace Engineering, North Carolina State University, Raleigh, NC 27695

Yong Zhu¹

Department of Mechanical and Aerospace Engineering, North Carolina State University, Raleigh, NC 27695
e-mail: yong_zhu@ncsu.edu

Interfacial shear stress transfer of a monolayer graphene on top of a polymer substrate subjected to uniaxial tension was investigated by a cohesive zone model integrated with a shear-lag model. Strain distribution in the graphene flake was found to behave in three stages in general, bonded, damaged, and debonded, as a result of the interfacial stress transfer. By fitting the cohesive-shear-lag model to our experimental results, the interface properties were identified including interface stiffness (74 Tpa/m), shear strength (0.50 Mpa), and mode II fracture toughness (0.08 N/m). Parametric studies showed that larger interface stiffness and/or shear strength can lead to better stress transfer efficiency, and high fracture toughness can delay debonding from occurring. 3D finite element simulations were performed to capture the interfacial stress transfer in graphene flakes with realistic geometries. The present study can provide valuable insight and design guidelines for enhancing interfacial shear stress transfer in nanocomposites, stretchable electronics and other applications based on graphene and other 2D nanomaterials.

[DOI: 10.1115/1.4029635]

Keywords: graphene, interface, cohesive zone, shear-lag

1 Introduction

Graphene holds a promising potential for a wide range of applications due to its excellent electrical, optical, and mechanical properties. For example, it has been considered as a potential alternative for silicon in flexible and stretchable electronics [1–4]. Another emerging application of graphene is nanocomposites [5–7], since it has been reported that graphene possesses a Young's modulus of 1 Tpa and intrinsic strength beyond 100 Gpa [8–11]. This high modulus and strength make it an exceptional candidate as the reinforcement of composite materials. In such applications as stretchable electronic devices and nanocomposites, graphene is usually placed on top of (or embedded within) a polymeric substrate (or matrix) [1,2,5–7]. By analogy to thin film/substrate and carbon nanotube/matrix systems [12–15], one of the most critical issues that determines the performance and reliability of these applications lies in the interface mechanical properties, especially the shear interaction between graphene and polymer substrate (or matrix). While graphene is very strong, a weak interface may damage and fail [5,16]. Compared to the extensive investigations that have been devoted to thin film/substrate and carbon nanotube/matrix interfaces, however, interfacial stress transfer at the graphene/polymer interface has been rarely studied.

Several recent experiments have been reported on the interfacial stress transfer at the graphene/polymer interface [16–21]. In these experiments, a monolayer graphene flake was either placed on top of or embedded within a polymer substrate. When the polymer substrate was subjected to uniaxial tension, the graphene flake underwent tensile strain as a result of the interfacial stress transfer. Raman spectroscopy was used in these studies to measure the strain in the graphene; Raman peaks of carbon materials (e.g., graphene and carbon nanotubes [22]) shift with strain, enabling

quantitative measurement of strain in such materials. Interfacial properties can be deduced from these measurements with the aid of shear-lag type of models. When the substrate is subjected to a relatively small strain, the classical shear-lag model is valid with a linear shear stress—sliding displacement relationship (perfectly bonded) [16]. When subjected to a larger strain level, a nonlinear shear-lag model was proposed assuming a constant shear stress (i.e., shear strength) is reached beyond the linear stage [18].

Interfacial shear strength is one of the most important parameters to characterize interface mechanical properties. Gong et al. [16] found that the interfacial shear strength of a monolayer graphene encapsulated between poly(methyl methacrylate) and SU-8 was ~ 2.3 Mpa, while our previous study obtained a range (0.46–0.69 Mpa) between graphene and polyethylene terephthalate (PET) [18]. Another important interface parameter is fracture toughness. Though mode I fracture toughness (i.e., adhesion energy) has been reported for the interfaces between graphene and different substrate materials [23–27], mode II fracture toughness at the graphene interface (e.g., in the case of graphene sliding on a substrate) has not been reported.

Recent molecular dynamics (MD) simulations [28] suggested that damage and debonding could occur after the perfect bonding between graphene and polyethylene (PE) (note that no covalent bonding was assumed at the interface in the simulations). A cohesive law in shear mode extracted from the MD simulations has been implemented in a continuum model to predict mechanical response of nanocomposites [29]. Experimentally, Srivastava et al. [19] found interface debonding between graphene and polydimethylsiloxane in the nanocomposites using scanning electron microscopy and Raman spectroscopy. Therefore, it is of relevance to consider damage and debonding beyond the perfect bonding.

This paper reports a study on the interfacial stress transfer of a monolayer graphene on top of a commonly used polymer substrate, PET. Cohesive zone model considering damage and debonding was integrated with shear-lag model to identify key interface parameters including interface stiffness, interface shear strength, and interface fracture toughness (mode II) and to study the effects of these parameters on the mechanical properties of the

¹Corresponding author.

Contributed by the Applied Mechanics Division of ASME for publication in the JOURNAL OF APPLIED MECHANICS. Manuscript received November 20, 2014; final manuscript received January 19, 2015; published online January 30, 2015. Editor: Yonggang Huang.

monolayer graphene. This paper is organized as follows: In Sec. 2, a cohesive zone model combined with a shear-lag model is developed [30–32]. The interface behavior can be divided into three stages: bonded, damaged, and debonded. Two critical strains, for damage initiation and debonding initiation, are identified. In Sec. 3, the interface parameters in the cohesive-shear-lag model are determined by fitting to available experimental results. Then, parametric studies are conducted to evaluate the effects of the interface parameters. Finite element analysis (FEA) implementing the cohesive zone model is developed, which is particularly useful to simulate the graphene flaks with realistic, complex geometries. Finally, conclusions of this study are drawn in Sec. 4.

2 Cohesive Zone Model Integrated With Shear-Lag Analysis

2.1 Cohesive Zone Model. Cohesive zone model has been widely used in the study of crack initiation and propagation at the interface in fiber reinforced composites, coating adhesives, and many other bimaterial systems [33,34]. In a graphene/polymer system, a large fracture process zone may develop at the interface under stretching, where the cohesive traction is assumed to vary along the fracture process zone but depend only on the local sliding and/or opening [35]. Thus, the cohesive law can be considered as a basic fracture property. While the specific form of a cohesive zone model differs from one to another [35–37], a typical cohesive zone model takes a similar feature of traction–separation relationship, of which the traction first increases with the separation until reaching a critical value, and then decreases with further increase of the separation till vanishing.

In the present study, a simple form of bilinear cohesive zone model [36] is adopted (as shown in Fig. 1). A schematic illustration of the problem is shown in Fig. 2. Since the interface sliding between graphene flake and substrate during uniaxial tension is attributed to mode II fracture, the traction–separation law can therefore be reduced to the relationship between shear traction and sliding displacement. As can be seen from Fig. 1, the shear traction first increases linearly with a constant stiffness K_0 , until reaching the so-called shear strength τ_{\max} , and then decreases with another constant slope while the sliding displacement further increases. Finally, it vanishes at a critical failure displacement δ_f then the interface loses its load carrying capacity. It has been accepted that the two of the most important parameters that define the cohesive law are the fracture toughness G_c , of which the magnitude equals to the area under the traction–separation curve, and the shear strength τ_{\max} . The effects of these two parameters and interface stiffness will be discussed later. It should be noted that in the present study, both graphene and PET substrates are assumed to be isotropic and linear elastic. Nonlinear effects will be taken into account in future works. The formula of the bilinear cohesive law is briefly given as follows:

The fracture toughness G_c takes the form of

$$G_c = \frac{1}{2} \tau_{\max} \delta_f \quad (1)$$

Before reaching the first critical sliding displacement δ_i , which corresponds to the shear strength τ_{\max} , the shear traction τ is linearly related to the sliding displacement as

$$\tau = K_0 \delta \quad (2)$$

where δ is the sliding displacement. After exceeding δ_i , the slope can be determined as $\tau_{\max}/(\delta_i - \delta_f)$; therefore, the shear traction can be expressed as

$$\tau = \tau_{\max} \frac{\delta_f - \delta}{\delta_f - \delta_i} \quad (3)$$

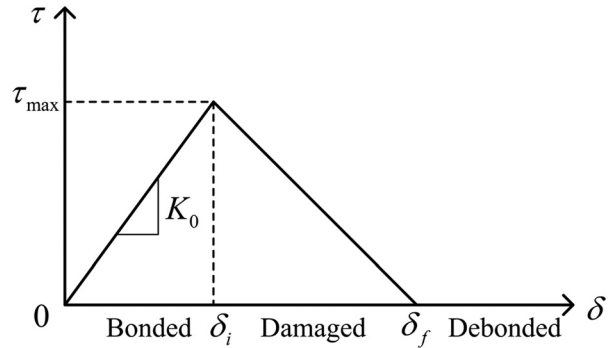


Fig. 1 Bilinear cohesive law

The shear stress becomes zero if further sliding occurs. For $\delta_i < \delta < \delta_f$, a damage variable, D , is defined to describe the damage evolution at the interface $D = \delta_f(\delta - \delta_i)/(\delta_f - \delta_i)$ [30].

2.2 Shear-Lag Model. In the present analysis, as shown in Fig. 2, only half of the graphene/substrate system in the horizontal (x) direction is considered for the sake of symmetry. The monolayer graphene holds a half-length L in the x direction with $x = 0$ at the center of the graphene.

Shear-lag model [38] has recently been used to describe the shear stress transfer between a monolayer graphene and a substrate [16–18]. Under uniaxial tensile loading condition, the tensile stress transfers from the substrate to the graphene by means of interfacial shear stress. The graphene holds a Young's modulus of $E_g (= 1 \text{ Tpa})$ [8], so the constitutive equation of graphene can be given as $\sigma = E_g \varepsilon$, where σ and ε denote the axial stress and strain in the graphene, respectively.

The equilibrium condition for the graphene in the tensile direction leads to

$$\tau = -h \frac{d\sigma}{dx} \quad (4)$$

where $h = 0.35 \text{ nm}$ is the graphene thickness.

The sliding displacement at the interface can be expressed as [35]

$$\delta = u_m - u_g \quad (5)$$

where $u_m = \varepsilon_m x$ and $u_g = \varepsilon x$, represents the displacement of substrate and graphene flake, respectively.

Combining Eqs. (4) and (5) relates shear stress with sliding displacement as

$$\tau = E_g h \frac{d^2 \delta}{dx^2} \quad (6)$$

where τ can be obtained from the cohesive law as will be discussed later.

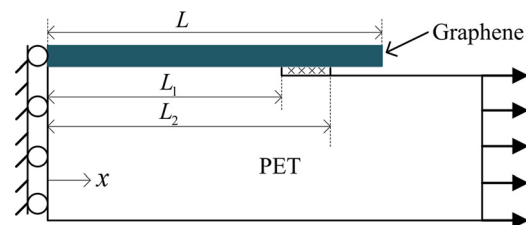


Fig. 2 Schematic diagram of the monolayer graphene/PET configuration under uniaxial tension

2.3 Integrated Cohesive Zone Model With Shear-Lag

Analysis. Upon uniaxial tension on the substrate, the sliding displacement increases between graphene and substrate. The shear stress at the interface first increases linearly and then decreases linearly till vanishing according to the bilinear cohesive zone model. The three stages of the interface behavior are in accordance with the three parts shown in Fig. 2: first part—bonded ($0 < x < L_1$), second part—damaged ($L_1 < x < L_2$), and third part—debonded ($L_2 < x < L$). Note that L_1 , L_2 , and L are equal at the undeformed state.

During the first stage when the applied strain is relatively small, the sliding displacement in the entire graphene is smaller than δ_i , so the graphene/substrate interface can be considered as perfectly bonded. The shear stress is given by Eq. (2), substituting which into Eq. (6) yields the following ordinary differential equation:

$$\frac{d^2\delta}{dx^2} = \frac{K_0}{E_g h} \delta \quad (7)$$

Applying the boundary conditions $\sigma = 0$ at $x = L$ and $u_g = 0$ at $x = 0$, Eq. (7) can be solved as

$$\delta = \frac{\varepsilon_m}{\beta \cosh(\beta L)} \sinh(\beta x) \quad (8)$$

where $\beta = \sqrt{K_0/E_g h}$ is the shear-lag parameter. The axial strain in the graphene is obtained as

$$\varepsilon = \varepsilon_m \left(1 - \frac{\cosh(\beta x)}{\cosh(\beta L)} \right) \quad (9)$$

This result is the same as the classical shear-lag model. However, here only one parameter, K_0 , needs to be determined.

A shear strength criterion can be set beyond which the interface goes into damage. At this point, the sliding displacement at the very edge of the graphene should be equal to δ_i . Thus, from Eq. (8), the first critical strain, which is associated with damage initiation, is given by

$$\varepsilon_{c1} = \delta_i \beta \coth(\beta L) \quad (10)$$

As the applied strain to the substrate further increases, the sliding displacement increases. The interface behavior may include two parts. In the first part, with length L_1 as shown in Fig. 2, the sliding displacement is smaller than δ_i , thus the interface is still perfectly bonded. At the point of $x = L_1$, the sliding displacement is exactly equal to δ_i . With this boundary condition, the axial strain in the bonded part can be obtained as

$$\varepsilon = \varepsilon_m - \delta_i \beta \frac{\cosh(\beta x)}{\sinh(\beta L_1)} \quad (11)$$

In the second part, the interface is damaged because the sliding displacement exceeds δ_i . The shear stress is thus given by Eq. (3), substituting which into Eq. (6) leads to

$$\frac{d^2\delta}{dx^2} = \alpha^2 (\delta_f - \delta) \quad (12)$$

where $\alpha = \sqrt{\tau_{\max}/(E_g h(\delta_f - \delta_i))}$. Applying the boundary condition $\delta = \delta_i$ and continuity condition $\sigma_{L_1}^+ = \sigma_{L_1}^-$ at $x = L_1$, Eq. (12) can be solved as

$$\delta = A \cos(\alpha(L_1 - x)) + B \sin(\alpha(x - L_1)) + \delta_f \quad (13)$$

where $A = \delta_i - \delta_f$ and $B = \delta_i \beta \coth(\beta L_1)/\alpha$. The axial strain in the damaged part takes the form of

$$\varepsilon = \varepsilon_m + A\alpha \sin(\alpha(x - L_1)) - B\alpha \cos(\alpha(x - L_1)) \quad (14)$$

where L_1 can be determined by applying boundary condition $\sigma = 0$ at $x = L$, given as

$$A\alpha \sin(\alpha(L - L_1)) - B\alpha \cos(\alpha(L - L_1)) = -\varepsilon_m \quad (15)$$

For the graphene to debond from the substrate, the sliding displacement at the edge of the graphene needs to achieve the critical failure separation δ_f . Hence, by setting $\delta = \delta_f$ at $x = L$, Eq. (13) becomes

$$A \cos(\alpha(L - L_1)) + B \sin(\alpha(L - L_1)) = 0 \quad (16)$$

This equation gives a critical value of L_1 , denoted as L_{1c} . The corresponding strain applied to the substrate can be considered as the second critical strain, denoted by ε_{c2} , which can be determined by Eq. (15) after L_{1c} is determined.

Further increase in the strain applied to the substrate leads to debonding from the graphene edges to the center. Thus, the interface involves a debonded part. Now the bonded part and damaged part have total length of L_2 as shown in Fig. 2. In this case, the strain in the bonded part and damaged part still takes the same form of Eqs. (11) and (14), respectively. In the debonded part, the strain in the graphene becomes zero. The length of L_1 and L_2 can be obtained simply by solving Eqs. (15) and (16) simultaneously by substituting L with L_2 .

For completeness, the present model is briefly compared to the nonlinear shear-lag analysis presented in our previous work [18]. In both cases, constant interface stiffness is assumed in the perfectly bonded stage. In the nonlinear shear-lag analysis, beyond the perfectly bonded stage with constant interface stiffness, the shear stress is assumed constant. By contrast, in the present model, two stages (damage and debonding) are introduced; the shear stress linearly decreases till vanishing with the increasing sliding displacement. As a result of such a difference, the mode II fracture toughness can be evaluated in the present analysis, which is not possible in the nonlinear shear-lag analysis. In addition, the strain distribution after damage and debonding can be predicted in the present analysis. As to fitting the experimental results in terms of strain distribution in graphene, the difference between the two models is modest when the graphene is short and the applied strain to the substrate is small, which is the case of our experiments [18]. However, a distinction between the two models can be seen for a larger graphene length and/or a larger strain to the substrate, as will be shown later.

3 Results and Discussion

3.1 Experimental Results and Parameters Identification.

In our experiment, a PET substrate with a monolayer graphene on top was uniaxially stretched by a small-scale mechanical testing stage. Raman spectroscopy was used to measure the local strains along the graphene flake at different applied strain levels. For more details on the experiments, see Ref. [18]. The measured strain distribution in a monolayer graphene with a length of 21.8 μm is shown in Fig. 3, for six different applied strain levels, 0.2%, 0.4%, 0.6%, 0.8%, 1.0%, and 1.2%. It can be seen that when the applied strain is as small as 0.2%, strain distribution along the graphene shows a typical characteristic of the classical shear-lag model. As a consequence, the entire interface can be considered in its perfectly bonded stage at this strain level. By fitting the experimental results at $\varepsilon_m = 0.2\%$ with Eq. (9), the interface stiffness K_0 was found to be 74 Tpa/m.

When the applied strain further increases, though the center strain in the graphene is approximately equals to the applied strain in the substrate, the shear stress at the graphene edges tends to approach a constant value or even decrease as shown by the slope of the strain distribution in Fig. 3. This means that damage has

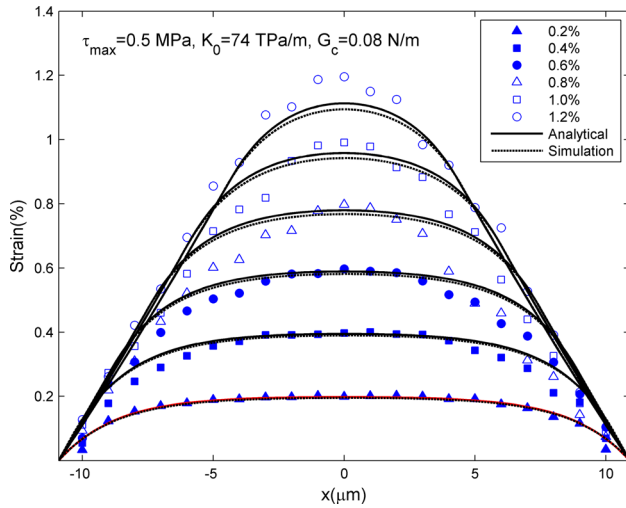


Fig. 3 Strain distribution along the length of a graphene flake. Symbols represent experimental data, solid lines are the analytical solution of the cohesive-shear-lag model and dashed lines are the FEA simulation. Red line (0.2% strain) indicates that the interface is perfectly bonded while blank lines indicate that damage occurs.

initiated gradually from graphene edges. In addition, the shear stress does not vanish even when the applied strain is as large as 1.2%, which implies that no debonding has occurred. Accordingly, the interface can be divided into two regions at these strain levels: The middle of the interface is perfectly bonded while the rest of the interface has been damaged. By fitting the experimental results to Eqs. (11) and (14), the shear strength is found to be 0.50 MPa and the mode II interface fracture toughness ~ 0.08 N/m. It should be noted that since the measured graphene flake was quite short and debonding did not occur, the obtained fracture toughness value should be treated as an estimate. The fitted results are shown in Fig. 3 by solid lines, where a very good agreement is obtained except some local discrepancies. The fitting highlighted in red is when the applied strain level was below the first critical strain as determined by Eq. (10) (i.e., the entire interface was perfectly bonded).

3.2 Finite Element Analysis. For the potential applications of graphene in stretchable electronics and nanocomposites among

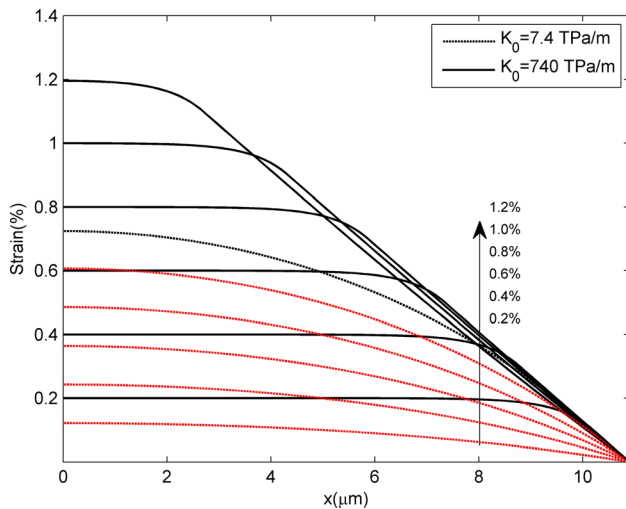


Fig. 4 Effect of interface stiffness. Red lines indicate that the interface is perfectly bonded while blank lines indicate that damage occurs. When $K_0 = 740$ TPa/m, the first critical strain $\epsilon_{c1} = 0.10\%$; when $K_0 = 7.4$ TPa/m, $\epsilon_{c1} = 1.07\%$.

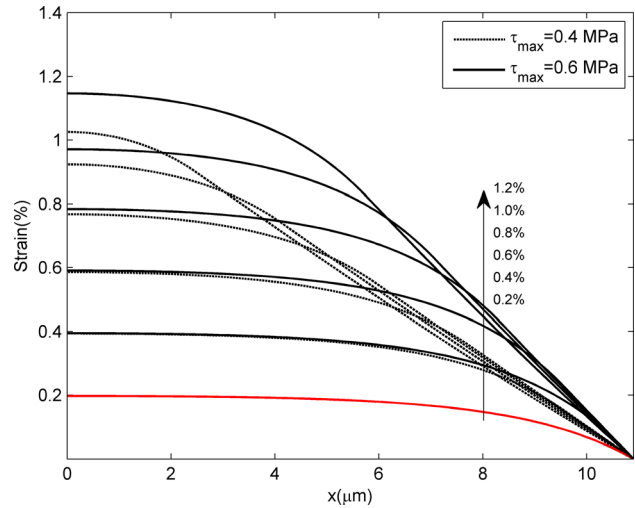


Fig. 5 Effect of interfacial shear strength. Red lines indicate that the interface is perfectly bonded while blank lines indicate damage occurs. When $\tau_{max} = 0.4$ MPa, $\epsilon_{c1} = 0.25\%$; and when $\tau_{max} = 0.6$ MPa, $\epsilon_{c1} = 0.37\%$.

others, it is important to predict the mechanical behavior of graphene flakes of realistic, often complex shapes. With this motivation, FEA models were developed.

In a 2D model, CPS4R element in ABAQUS 6.10 [39] was employed to model both the graphene layer and the PET substrate. Both materials are considered isotropic, linearly elastic with the following properties: Young's modulus 1 TPa and 3 GPa, Poisson's ratio 0.165 and 0.39, for graphene and PET, respectively. COH2D4 element with the bilinear cohesive law (Fig. 1) was used to model the interface. The material parameters, in the shear direction, incorporated in the cohesive law were those obtained in Sec. 3.1 through fitting. As to the normal direction, the interface strength and fracture toughness were assumed to be equal to those in the shear direction. The normal stiffness was considered as a penalty parameter, with a large value to prohibit normal direction penetration in compression and separation in tension. Benzeggagh-Kenane fracture criterion was used to define the initiation of the debonding, considering the mixed mode behavior in the simulation. The damage variable D was used to track the interface sliding status (e.g., bonded, damaged, or debonded). The numerical results of strain distribution along the graphene at different applied strain

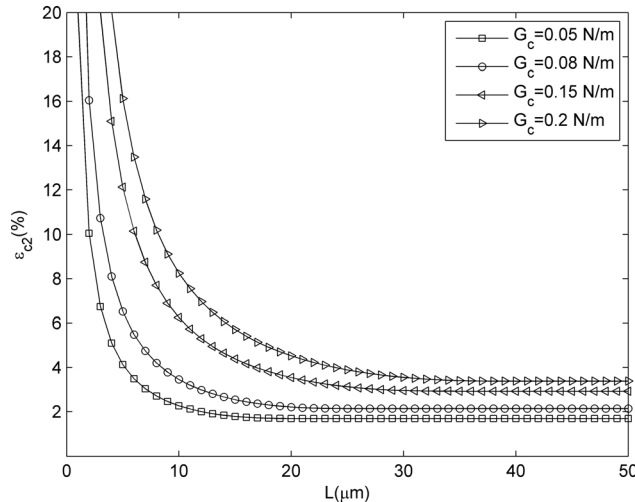


Fig. 6 Effect of graphene length and interface fracture toughness on the second critical strain defined in Sec. 2.3

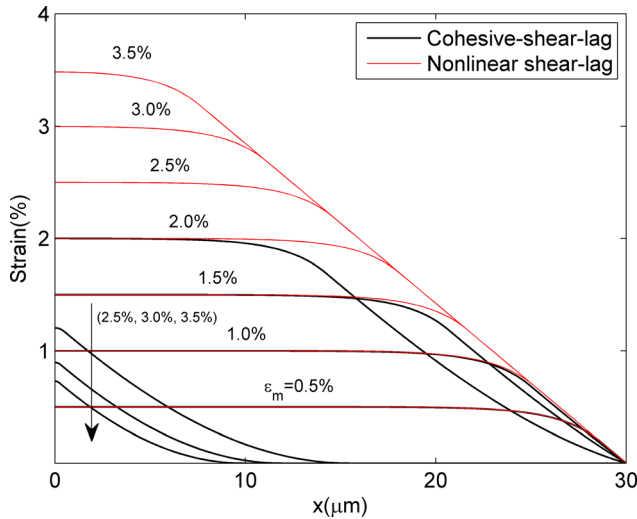


Fig. 7 Strain distribution in a graphene flake with length of 60 μm using the cohesive-shear-lag model and the nonlinear shear-lag model

levels are shown in Fig. 3. It can be seen that the simulations agree very well with both the experiments and analytical solutions.

To account for the complex geometries of the graphene that might occur in real applications, a 3D model was also developed. In this case, M3D4R element was employed to model the graphene layer and C3D8R element to model the PET substrate, while COH3D8 element was used for the interface.

3.3 Interface Properties and Their Effects. With the interface properties identified in Sec. 3.1, the effects of interface stiffness, shear strength, and fracture toughness on interfacial stress transfer and damage/debonding propagation will be discussed in this section.

3.3.1 Effect of Interface Stiffness. To show the effects of interface stiffness and shear strength on strain distribution in a

graphene flake, graphene length of 21.8 μm was used as in our experiment. As will be shown later, debonding does not happen for such a small graphene length as long as the applied strain is not exceedingly high. Thus, the graphene consists of two parts: fully bonded part and damaged part. The effect of interface stiffness can be studied by keeping shear strength (0.50 Mpa) and fracture toughness (0.08 N/m) constant. As can be seen from Fig. 4, while the first critical strain ϵ_{c1} decreases with increasing interface stiffness, the plateau strain built up at the graphene center increases dramatically and the length of the plateau region increases too.

3.3.2 Effect of Interface Shear Strength. By varying its magnitude (0.4 and 0.6 Mpa) while keeping interface stiffness (74 Tpa/m) and fracture toughness (0.08 N/m) constant, the effect of interface shear strength on graphene strain distribution is shown in Fig. 5. It can be seen that while the shear strength does not have much effect at small applied strains (e.g., 0.2%), a larger normal stress ensues with increasing shear strength in the graphene at larger applied strains. In addition, a larger shear strength results in a larger first critical strain ϵ_{c1} , which means that the interface can undergo a larger substrate strain before damage happens.

3.3.3 Effect of Interface Fracture Toughness. In contrast to interface shear strength and interface stiffness that affect strain distribution in both the fully bonded part and damaged part, interface fracture toughness G_c only comes into play after damage happens. In this case, before debonding, the interface includes two parts: $x < L_1$ (perfectly bonded) and $x > L_1$ (damaged). The length L_1 can be obtained from Eq. (15). It shows that with the increase of the applied substrate strain, the length L_1 decreases and $(L - L_1)$ increases. However, there is an upper limit, ϵ_{c2} , for the applied strain, beyond which the shear stress at graphene edges becomes zero and debonding occurs. The effect of interface fracture toughness and graphene length on ϵ_{c2} is shown in Fig. 6. Obviously, with increasing interface fracture toughness, ϵ_{c2} increases (i.e., delays debonding at the interface). Another observation is that graphene of smaller length are highly resistant to debonding because ϵ_{c2} attains a very large value. With increasing

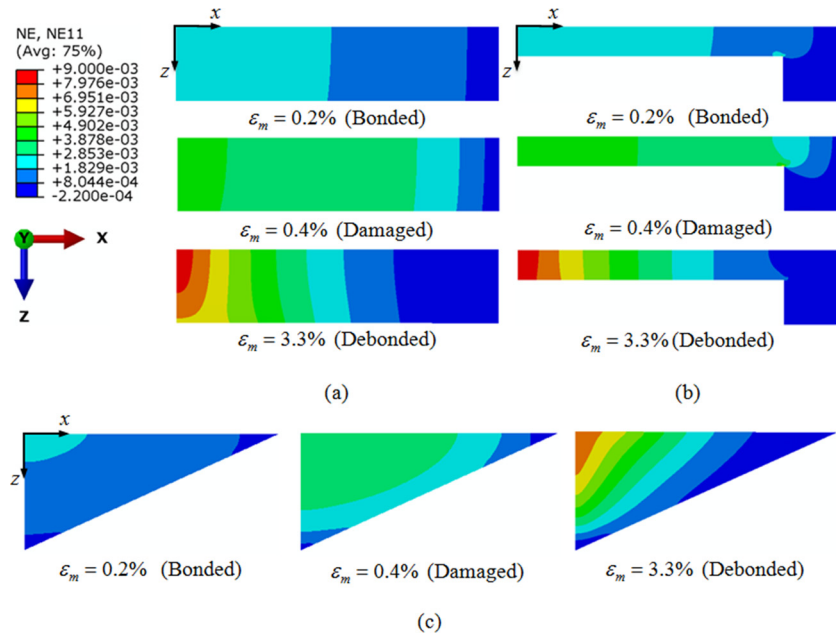


Fig. 8 Normal strain distribution in (a) rectangular, (b) H shaped, and (c) triangular graphene flakes under different applied substrate strain levels (in x direction). Graphene length is 21.8 μm and width is 5 μm in all cases. A quarter of the model is used for the rectangular and H shapes, and a half for the triangular shape due to symmetry.

graphene length, ε_{c2} decreases and approaches a nearly constant value.

3.4 Graphene Debonding. When the applied substrate strain exceeds the second critical strain ε_{c2} , a debonded part ($L_2 < x < L$) initiates from the graphene edges. To investigate the interface stress transfer at this stage, strain distribution at different applied strain levels (from 0.5% to 3.5%) in a graphene of 60 μm in length is shown in Fig. 7 (note that only half of the graphene length is shown). The reason to choose 60 μm length is because ε_{c2} for this length achieves an almost constant value as can be seen from Fig. 6 (with a corresponding $\varepsilon_{c2} = 2.14\%$ for $G_c = 0.08$ N/m). The most striking feature in this case is that, when the applied strain exceeds ε_{c2} , there does not exist a plateau strain in the graphene center. Indeed, the graphene center strain gradually decreases with the increasing substrate strain. On the other hand, at graphene edges, the strain becomes zero; the length of the debonded part increases with the increasing substrate strain because debonding propagates from the graphene edges to the center. For comparison purpose, the results predicted by the nonlinear shear-lag model [18] are also presented in Fig. 7.

Before debonding occurs, the normal stress in graphene is simply the integration of interface shear stress over the distance from the edge according to Eq. (4). Therefore, the longer the graphene, the more efficient interfacial stress transfer is (assuming the interfacial properties unchanged). But after debonding occurs, the graphene length becomes irrelevant in the present model in terms of interfacial stress transfer. According to Eqs. (15) and (16), the length of the bonded and damaged parts remains constant, regardless of the total graphene length. To achieve better interfacial stress transfer, it is advisable to keep the applied strain to the substrate below the critical strain for debonding, ε_{c2} , for a given graphene length, as shown in Fig. 6.

3.5 FEA of Complex Graphene Geometries. In real applications, graphene flakes might have complex shapes rather than the idealized rectangle one analyzed so far. The complex shapes could be a result of the desired device patterning or the mechanical exfoliation method used to prepare the flakes. Therefore, it is of relevance to investigate how the geometry affects the interfacial stress transfer. In this section, three graphene geometries, rectangular, "H" shaped, and triangular, were simulated using FEA. The H shaped graphene flakes have been used in graphene-based transistors [40], while the triangular shape is an exaggerated representation of the mechanically exfoliated flakes that are typically irregular. The strain distribution results under three stages, bonded, damaged, and debonded, are shown in Fig. 8. It can be seen that the longitudinal strain always first builds at the graphene edge and increases toward the largest value in the center. When debonding is initiated, the zero strain zone in the graphene propagates from the edge to the center. The nonuniform strain distribution in the transverse direction is due to transverse shear caused by Poisson's effect as well as the complex geometry.

4 Conclusions

A cohesive-shear-lag model was developed to investigate the interfacial shear stress transfer of a monolayer graphene on top of a PET substrate. Strain distribution in the graphene flake was found to behave in three stages in general, bonded, damaged, and debonded, depending on the interface properties and the graphene length. By fitting the available experimental data, the interface stiffness, shear strength, and mode II fracture toughness were identified with the values of 74 Tpa/m, 0.50 Mpa, and 0.08 N/m, respectively, for the graphene/PET interface. Parametric studies showed that larger interface stiffness and/or shear strength can lead to higher stress transfer efficiency, while high fracture toughness can delay debonding. Compared to the nonlinear shear-lag model [18], the present model defines two stages, damage and

debonding, beyond perfect bonding, which might be relevant for a large graphene length and/or a large substrate strain. 3D FEA was performed to capture the interfacial stress transfer in graphene flakes with complex geometries. The analytical and FEA models can be readily extended to study other two-dimensional nanomaterials (e.g., hexagonal boron nitride, molybdenum disulfide, and silicene) on polymer substrates. Our experiment did not observe sliding due to the relatively small graphene size (prepared by the scotch-tape method). Future work would extend the experiment to larger sample size (e.g., prepared by the chemical vapor deposition method) where damage and debonding at the graphene/PET interface is more likely.

Acknowledgment

This work was supported in part by the National Science Foundation through the EFRI program (EFRI-1240438). G.G. would like to acknowledge a scholarship from the China Scholarship Council.

References

- [1] Wang, Y., Yang, R., Shi, Z. W., Zhang, L. C., Shi, D. X., Wang, E., and Zhang, G. Y., 2011, "Super-Elastic Graphene Ripples for Flexible Strain Sensors," *ACS Nano*, **5**(5), pp. 3645–3650.
- [2] Raju, A. P. A., Lewis, A., Derby, B., Young, R. J., Kinloch, I. A., Zan, R., and Novoselov, K. S., 2014, "Wide-Area Strain Sensors Based Upon Graphene-Polymer Composite Coatings Probed by Raman Spectroscopy," *Adv. Funct. Mater.*, **24**(19), pp. 2865–2874.
- [3] Rogers, J. A., Someya, T., and Huang, Y., 2010, "Materials and Mechanics for Stretchable Electronics," *Science*, **327**(5973), pp. 1603–1607.
- [4] Kim, R.-H., Bae, M.-H., Kim, D. G., Cheng, H., Kim, B. H., Kim, D.-H., Li, M., Wu, J., Du, F., Kim, H.-S., Kim, S., Estrada, D., Hong, S. W., Huang, Y., Pop, E., and Rogers, J. A., 2011, "Stretchable, Transparent Graphene Interconnects for Arrays of Microscale Inorganic Light Emitting Diodes on Rubber Substrates," *Nano Lett.*, **11**(9), pp. 3881–3886.
- [5] Young, R. J., Kinloch, I. A., Gong, L., and Novoselov, K. S., 2012, "The Mechanics of Graphene Nanocomposites: A Review," *Compos. Sci. Technol.*, **72**(12), pp. 1459–1476.
- [6] Ramanathan, T., Abdala, A. A., Stankovich, S., Dikin, D. A., Herrera Alonso, M., Piner, R. D., Adamson, D. H., Schniepp, H. C., Chen, X., Ruoff, R. S., Nguyen, S. T., Aksay, I. A., Prud'Homme, R. K., and Brinson, L. C., 2008, "Functionalized Graphene Sheets for Polymer Nanocomposites," *Nat. Nanotechnol.*, **3**(6), pp. 327–331.
- [7] Rafiee, M. A., Rafiee, J., Wang, Z., Song, H., Yu, Z.-Z., and Koratkar, N., 2009, "Enhanced Mechanical Properties of Nanocomposites at Low Graphene Content," *ACS Nano*, **3**(12), pp. 3884–3890.
- [8] Lee, C., Wei, X. D., Kysar, J. W., and Hone, J., 2008, "Measurement of the Elastic Properties and Intrinsic Strength of Monolayer Graphene," *Science*, **321**(5887), pp. 385–388.
- [9] Lee, G. H., Cooper, R. C., An, S. J., Lee, S., van der Zande, A., Petrone, N., Hammerberg, A. G., Lee, C., Crawford, B., Oliver, W., Kysar, J. W., and Hone, J., 2013, "High-Strength Chemical-Vapor Deposited Graphene and Grain Boundaries," *Science*, **340**(6136), pp. 1073–1076.
- [10] Zhang, P., Ma, L., Fan, F., Zeng, Z., Peng, C., Loya, P. E., Liu, Z., Gong, Y., Zhang, J., Zhang, X., Ajayan, P. M., Zhu, T., and Lou, J., 2014, "Fracture Toughness of Graphene," *Nat. Commun.*, **5**, p. 3782.
- [11] Rasool, H. I., Ophus, C., Klug, W. S., Zettl, A., and Gimzewski, J. K., 2013, "Measurement of the Intrinsic Strength of Crystalline and Polycrystalline Graphene," *Nat. Commun.*, **4**, p. 2881.
- [12] Jia, Y. Y., Chen, Z. R., and Yan, W. Y., 2014, "A Numerical Study on Carbon Nanotube-Hybridized Carbon Fibre Pullout," *Compos. Sci. Technol.*, **91**, pp. 38–44.
- [13] Kulkarni, M., Carnahan, D., Kulkarni, K., Qian, D., and Abot, J. L., 2010, "Elastic Response of a Carbon Nanotube Fiber Reinforced Polymeric Composite: A Numerical and Experimental Study," *Composites Part B*, **41**(5), pp. 414–421.
- [14] Toth, F., Rammerstorfer, F. G., Cordill, M. J., and Fischer, F. D., 2013, "Detailed Modelling of Delamination Buckling of Thin Films Under Global Tension," *Acta Mater.*, **61**(7), pp. 2425–2433.
- [15] Sun, J. Y., Lu, N. S., Yoon, J., Oh, K. H., Suo, Z. G., and Vlassak, J. J., 2012, "Debonding and Fracture of Ceramic Islands on Polymer Substrates," *J. Appl. Phys.*, **111**(1), p. 013517.
- [16] Gong, L., Kinloch, I. A., Young, R. J., Riaz, I., Jalil, R., and Novoselov, K. S., 2010, "Interfacial Stress Transfer in a Graphene Monolayer Nanocomposite," *Adv. Mater.*, **22**(24), pp. 2694–2697.
- [17] Young, R. J., Gong, L., Kinloch, I. A., Riaz, I., Jalil, R., and Novoselov, K. S., 2011, "Strain Mapping in a Graphene Monolayer Nanocomposite," *ACS Nano*, **5**(4), pp. 3079–3084.
- [18] Jiang, T., Huang, R., and Zhu, Y., 2014, "Interfacial Sliding and Buckling of Monolayer Graphene on a Stretchable Substrate," *Adv. Funct. Mater.*, **24**(3), pp. 396–402.

- [19] Srivastava, I., Mehta, R. J., Yu, Z.-Z., Schadler, L., and Koratkar, N., 2011, "Raman Study of Interfacial Load Transfer in Graphene Nanocomposites," *Appl. Phys. Lett.*, **98**(6), p. 063102.
- [20] Tsoukleri, G., Parthenios, J., Papagelis, K., Jalil, R., Ferrari, A. C., Geim, A. K., Novoselov, K. S., and Galiotis, C., 2009, "Subjecting a Graphene Monolayer to Tension and Compression," *Small*, **5**(21), pp. 2397–2402.
- [21] Yu, T., Ni, Z., Du, C., You, Y., Wang, Y., and Shen, Z., 2008, "Raman Mapping Investigation of Graphene on Transparent Flexible Substrate: The Strain Effect," *J. Phys. Chem. C*, **112**(33), pp. 12602–12605.
- [22] Zu, M., Li, Q., Zhu, Y., Zhu, Y., Wang, G., Byun, J.-H., and Chou, T.-W., 2013, "Stress Relaxation in Carbon Nanotube-Based Fibers for Load-Bearing Applications," *Carbon*, **52**, pp. 347–355.
- [23] Koenig, S. P., Boddeti, N. G., Dunn, M. L., and Bunch, J. S., 2011, "Ultrastrong Adhesion of Graphene Membranes," *Nat. Nanotechnol.*, **6**(9), pp. 543–546.
- [24] Zong, Z., Chen, C. L., Dokmeci, M. R., and Wan, K. T., 2010, "Direct Measurement of Graphene Adhesion on Silicon Surface by Intercalation of Nanoparticles," *J. Appl. Phys.*, **107**(2), p. 026104.
- [25] Yoon, T., Shin, W. C., Kim, T. Y., Mun, J. H., Kim, T. S., and Cho, B. J., 2012, "Direct Measurement of Adhesion Energy of Monolayer Graphene As-Grown on Copper and Its Application to Renewable Transfer Process," *Nano Lett.*, **12**(3), pp. 1448–1452.
- [26] Cao, Z., Wang, P., Gao, W., Tao, L., Suk, J. W., Ruoff, R. S., Akinwande, D., Huang, R., and Liechti, K. M., 2014, "A Blister Test for Interfacial Adhesion of Large-Scale Transferred Graphene," *Carbon*, **69**, pp. 390–400.
- [27] Boddeti, N. G., Koenig, S. P., Long, R., Xiao, J., Bunch, J. S., and Dunn, M. L., 2013, "Mechanics of Adhered, Pressurized Graphene Blisters," *ASME J. Appl. Mech.*, **80**(4), p. 040909.
- [28] Amnaya, P. A., Dimitris, C. L., and Daniel, C. H., 2009, "Modeling of Graphene–Polymer Interfacial Mechanical Behavior Using Molecular Dynamics," *Modell. Simul. Mater. Sci. Eng.*, **17**(1), p. 015002.
- [29] Safaei, M., Sheidaei, A., Baniassadi, M., Ahzi, S., Mosavi Mashhadi, M., and Pourboghraat, F., 2015, "An Interfacial Debonding-Induced Damage Model for Graphite Nanoplatelet Polymer Composites," *Comput. Mater. Sci.*, **96**(Pt. A), pp. 191–199.
- [30] Ryu, S. K., Jiang, T. F., Im, J., Ho, P. S., and Huang, R., 2014, "Thermomechanical Failure Analysis of Through-Silicon Via Interface Using a Shear-Lag Model With Cohesive Zone," *IEEE Trans. Device Mater. Reliab.*, **14**(1), pp. 318–326.
- [31] Yang, B., and Mall, S., 2003, "Cohesive-Shear-Lag Model for Cycling Stress–Strain Behavior of Unidirectional Ceramic Matrix Composites," *Int. J. Damage Mech.*, **12**(1), pp. 45–64.
- [32] De Lorenzis, L., and Zavarise, G., 2009, "Cohesive Zone Modeling of Interfacial Stresses in Plated Beams," *Int. J. Solids Struct.*, **46**(24), pp. 4181–4191.
- [33] Barenblatt, G. I., 1959, "The Formation of Equilibrium Cracks During Brittle Fracture. General Ideas and Hypotheses. Axially-Symmetric Cracks," *J. Appl. Math. Mech.*, **23**(3), pp. 622–636.
- [34] Dugdale, D. S., 1960, "Yielding of Steel Sheets Containing Slits," *J. Mech. Phys. Solids*, **8**(2), pp. 100–104.
- [35] Jiang, L. Y., Huang, Y., Jiang, H., Ravichandran, G., Gao, H., Hwang, K. C., and Liu, B., 2006, "A Cohesive Law for Carbon Nanotube/Polymer Interfaces Based on the van der Waals Force," *J. Mech. Phys. Solids*, **54**(11), pp. 2436–2452.
- [36] Alfano, G., 2006, "On the Influence of the Shape of the Interface Law on the Application of Cohesive-Zone Models," *Compos. Sci. Technol.*, **66**(6), pp. 723–730.
- [37] Needleman, A., 1990, "An Analysis of Tensile Decohesion Along an Interface," *J. Mech. Phys. Solids*, **38**(3), pp. 289–324.
- [38] Cox, H. L., 1952, "The Elasticity and Strength of Paper and Other Fibrous Materials," *Br. J. Appl. Phys.*, **3**(3), pp. 72–79.
- [39] ABAQUS, 2010, "ABAQUS 6.10 Documentation," Dassault Systemes Simulia Corp., Johnston, RI.
- [40] Lee, S. K., Kim, B. J., Jang, H., Yoon, S. C., Lee, C., Hong, B. H., Rogers, J. A., Cho, J. H., and Ahn, J. H., 2011, "Stretchable Graphene Transistors With Printed Dielectrics and Gate Electrodes," *Nano Lett.*, **11**(11), pp. 4642–4646.